ADVANCED ELECTRONIC MATERIALS Open Access
www.advelectronicmat.de

Aligned Permanent Magnet Made in Seconds–An In Situ Diffraction Study

*Amalie P. Laursen, Jens P. Frandsen, Priyank Shyam, Mathias I. Mørch, Frederik H. Gjørup, Harikrishnan Vijayan, Mads R. V. Jørgensen, and Mogens Christensen**

The synthesis of a strontium hexaferrite magnet is studied using in situ synchrotron powder X-ray diffraction (PXRD) with a 16-ms time resolution. The precursor material is cold compacted shape-controlled goethite and strontium carbonate. The time evolution of the phases is modeled with sequential Rietveld refinements revealing that strontium hexaferrite forms within seconds at ≈1173 K. Texture analysis is performed on selected PXRD frames throughout the experiment, and the preferred orientation introduced by cold-pressing goethite prevails through the iron oxide phase transitions (goethite → hematite → strontium hexaferrite). Electron backscatter diffraction (EBSD) data on the final pellet confirms the preferred orientation observed with PXRD. The resulting magnet has respectable magnetic properties, considering the simplicity of the preparation method, with an energy product (BH_{max}) of 18.6(8) kJ m^{-3}.

1. Introduction

Advanced functional materials are defined by their structure and composition. Not only the atomic structure is important, but multiple hierarchical length scales determine their properties. Understanding the structure on all length scales, from the atomic level via nanoscale to the preferred crystallographic orientation on the microscale, is paramount for tailoring their properties and advancing materials technology. The challenge is inducing texture while maintaining the nanostructure and compacting the loose powder into dense materials for real-world applications. The ultrafast high-temperature sintering (UHS) technique allows for a wide range of functional materials to be sintered into dense pellets while maintaining their nanostructure.[1] Recently, UHS has been combined with in situ synchrotron powder X-ray diffraction (PXRD) allowing unprecedented insight into the sintering process with millisecond time resolution.[2] Here we employ UHS to follow a chemical reaction with in situ PXRD giving insight into all hierarchical length scales; atomic structure, nanosize, and crystallographic alignment. Permanent magnets are chosen as all length scales are important for the performance of the material.

Permanent magnets are highly important for modern society. With their ability to convert mechanical energy to electrical energy and vice versa, they find many applications, for example in motors, loudspeakers, and generators.[3] The quality of a permanent magnet is determined from the magnetic hysteresis curve, where the properties of interest are: saturation magnetization (M_s), coercivity (H_c), remanent magnetization (M_r), and energy product (BH_{max}). BH_{max} is considered a figure of merit for permanent magnets and is defined as the area of the largest square in the second quadrant of the B versus H hysteresis loop.[4] To achieve a substantial BH_{max}, all the magnetic properties must be optimized. This can only be done by controlling the structure of the magnet across multiple length scales. M_s is intrinsically linked to the atomic structure of the sample and is reduced by defects and impurities.[5,6] H_c depends on the atomic structure, a high crystalline anisotropy constant (K_1) is a prerequisite for high H_c, but H_c is also largely dependent on the crystallite size.[7] Stable Single Domain theory describes the existence of an optimal particle size (D_c), on the nanoscale, where H_c is maximized.[8,9] The D_c for spherical hexaferrite particles is reported to be ≈600 nm.[10] However, studies have shown the D_c of strontium hexaferrite with an anisotropic platelet shape is significantly smaller.[8] M_r is influenced by the orientation of the crystallites on the microscale.[11] A preferred orientation of the crystallites (or texture) along the magnetic easy axis is necessary to optimize M_r.[12] The degree of alignment is reflected in the squareness of the hysteresis curve (M_r/M_s).[13]

A. P. Laursen, J. P. Frandsen, P. Shyam, M. I. Mørch, F. H. Gjørup, H. Vijayan[+], M. R. V. Jørgensen, M. Christensen
Department of Chemistry and Interdisciplinary Nanoscience Center (iNANO)
Aarhus University
Langelandsgade 140, Aarhus 8000, Denmark
E-mail: mch@chem.au.dk
F. H. Gjørup, M. R. V. Jørgensen
MAX-IV Laboratory
Lund University
Fotongatan 2, Lund 224 84, Sweden

The ORCID identification number(s) for the author(s) of this article can be found under https://doi.org/10.1002/aelm.202400077

[+]Present address: IMDEA, Instituto Madrileño de Estudios Avanzados en Nanociencia, C/ Faraday 9, Madrid 28049, Spain

DOI: 10.1002/aelm.202400077

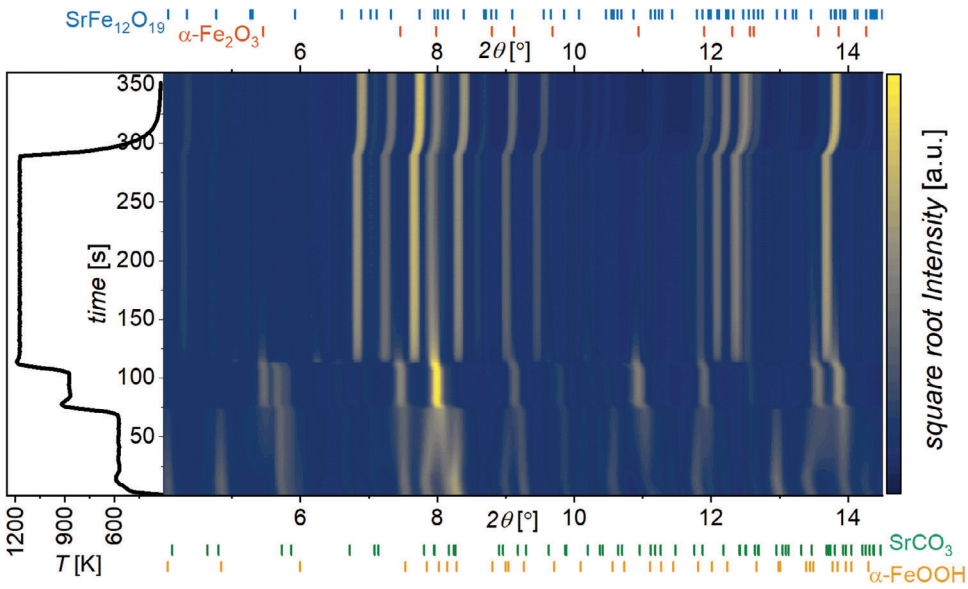

Figure 1. Integrated 1D PXRD patterns ($\lambda = 0.354$ Å) are shown as square root intensity with increasing experiment time along the *y*-axis. The figure on the left plots the temperature measured during the experiment. Bragg peak positions of the precursor phases have been given below for goethite (yellow) and strontium carbonate (green). Above are shown the Bragg peak positions of hematite (red) and strontium hexaferrite (blue).

The permanent magnet investigated in this study is strontium hexaferrite ($SrFe_{12}O_{19}$). With ≈1 million tons produced globally every year, hexaferrites constitute 80% of the permanent magnet market by weight, due to their low cost, good chemical stability, and relatively high Curie temperature.[3,14–16]

The industrial production of aligned hexaferrite magnets consists of several individual steps. First calcination of iron oxide and strontium carbonate to obtain the desired atomic structure (M_s), followed by milling to reduce the particle size (H_c), compaction in the presence of a magnetic field to align the particles (M_r), and a final heating step to recrystallize and sinter the particles.[17] Each processing/synthesis step is energy-intensive.[18] The immense scale of hexaferrite production makes it worthwhile to investigate energy-efficient alternative synthesis routes.

Previous studies have shown that aligned strontium hexaferrite magnets can be successfully produced in a single step, without applying an external magnetic field.[13,19] Here, the preferred orientation was introduced through cold compaction of anisotropic nanostructured iron oxyhydroxide/oxide precursors.

Goethite, in particular, excelled at producing aligned strontium hexaferrite magnets, which can be understood through a topotactic reaction.[13,19,20]

In this study, we seek to improve the understanding of the topotactic transformation of anisotropic nanosized goethite that leads to the preparation of highly aligned $SrFe_{12}O_{19}$. The in situ experiment allows us to follow the transformation over six orders of magnitude from atomic structure (10^{-10} m) via the nanostructure (10^{-7} m) to microstructural changes (10^{-4} m) with a time resolution of 16 ms. A cold compacted pellet of strontium carbonate and goethite was sintered using the UHS furnace AROS designed for in situ synchrotron experiments.[2] The in situ PXRD data was sequentially Rietveld refined to investigate changes in phases, unit cells, and crystallite sizes, and the texture was modeled for selected frames. Electron backscatter diffraction (EBSD) was used as a complementary method to PXRD for studying the texture and particle sizes of the resulting crystal grains in the magnet. The magnetic properties of the sample were characterized using vibrating sample magnetometry (VSM).

2. Results and Discussion

2.1. Qualitative Analysis

The time resolution of the in situ experiment allows for a detailed study of the occurring phase transitions. The 2D diffraction images were integrated using the MatFRAIA algorithm.[21] The Debye–Scherrer rings were integrated in the azimuthal range (η) from 0° to 180° into one bin with a 2θ step size of 0.015°. The heatmap and temperature plot in **Figure 1** provide an overview of the different stages of the reaction. Goethite (α-FeOOH, space group *Pnma*) is observed to go through the intermediary phase hematite (α-Fe_2O_3, space group *R*-3*c*) before reacting with strontium carbonate ($SrCO_3$, space group *Pmcn*) to form strontium hexaferrite ($SrFe_{12}O_{19}$, space group $P6_3/mmc$), which corroborates observations from literature.[20,22,23] The phase transition from goethite to hematite gradually starts at 573 K with rapid finalization as the temperature is increased to 873 K, leaving hematite as the only iron oxide. Strontium carbonate persists in the sample (e.g., the reflections at 5.7° and 5.9°) until the temperature is increased to 1173 K. At this point the strontium hexaferrite rapidly becomes the dominant phase forming from hematite and strontium carbonate. The formation of strontium hexaferrite coincides with a phase transformation in strontium carbonate from the orthorhombic space group *Pmcn* to the trigonal space group *R*-3*m* at ≈1173 K.[24] This is observed with the appearance of the reflection at 6.3° promptly disappearing as the phase is used up to form strontium hexaferrite.

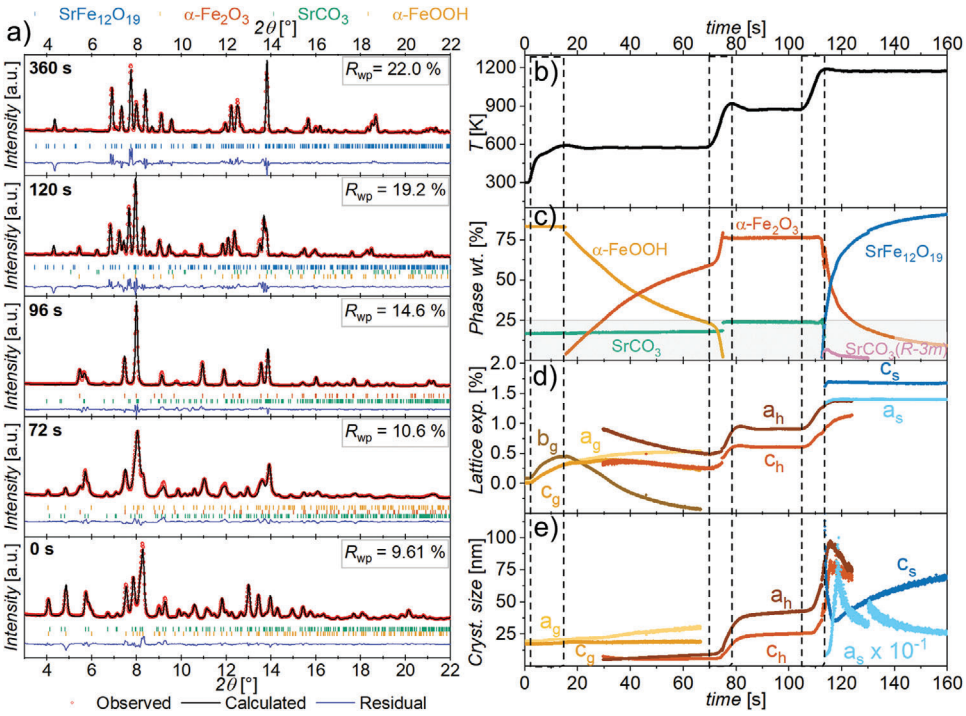

Figure 2. An overview of the results from the sequential Rietveld refinements of the first 10000 PXRD patterns ($\lambda = 0.354$ Å), from 0 to 160 s. a) refined PXRD data measured at time = 0, 72, 96, 120, and 360 s, b) temperature ramp in the first 160 s of the experiment, and c) weight percentages of α-FeOOH (yellow), α-Fe_2O_3 (red), $SrFe_{12}O_{19}$ (blue), and $SrCO_3$ in the Pmcn (green) and R-3m (pink). d) Lattice expansion where zero is defined from tabulated room temperature lattice parameters of the phases.[7,27] Different hues of yellow, red, and blue indicate the different lattice parameters (a–c), and the subscript indicates the phase g = α-FeOOH, h = α-Fe_2O_3, and s = $SrFe_{12}O_{19}$. e) The crystallite size along the *a*- and *c*-axis (The crystallite size along the *a*-axis of $SrFe_{12}O_{19}$ has been multiplied by 10^{-1} for better visualization). Only the lattice expansion and crystallite sizes of the major phases (phase percentage >25%) are included, as the parameters were unstable for minor phase fractions (see Supporting Information).

2.2. Sequential Refinement

The qualitative analysis provides an overview of the reaction, however, for a detailed understanding of the hierarchical structural changes during the experiment, sequential Rietveld refinements were performed in FullProf Suite.[25] Refinement details are given in Refinement Details—Sequential Refinements in FullProf Suite. It was chosen to refine the first 10000 PXRD patterns, corresponding to the first 160 s of the experiment, wherein all the phase transitions occur. Results from the sequential refinements have been presented in **Figure 2**, showing the phase fraction evolution, thermal expansion, and crystallite growth.

Refined PXRD patterns at *time* = 0, 72, 96, 120, and 360 s are given in Figure 2a, specifically chosen to visualize the agreeable fit of the multiphase model to the data. The agreement factor R_{wp} increases with increasing experiment time, along with an unidentified impurity observed at 13.6° in the final PXRD pattern of the experiment. Figure 2b–e illustrates the phase evolution with time and temperature. Unphysical shifts in weight fractions are noticed at time points where phases are introduced and removed from the model. Regions with a temperature increase have been emphasized with dashed lines.

The initial conversion rate of goethite to hematite is estimated to be 1% s^{-1} at 573 K and increases to 8% s^{-1} at 873 K leading to a rapid finalization of the phase transition. The formation of strontium hexaferrite also occurs rapidly once the temperature is increased to 1173 K. The phase goes from 0 to 50% in less than 4 s. The reaction occurs fast considering that conventional knowledge typically describes solid-state reactions as being "slow" with the necessity of heating the reactants for "prolonged periods."[26] The conventional knowledge is based on µm particles, however, in this study the precursor has nm dimensions, causing shorter diffusion pathways and consequently faster reaction kinetics.

The changes in unit cell dimensions, visualized in Figure 2d, have been calculated as percentage deviations from tabulated room temperature lattice parameters.[7,27] The initial thermal lattice expansion in goethite is followed by a significant decrease in the *b*-axis as goethite is dehydrated to form hematite. This agrees with the results by Gualtieri et al. and is explained by relaxations around the vacancies generated by proton migration in the structure as goethite decomposes.[22] For hematite, the initial decrease in lattice parameters could be explained by small nanocrystallites typically having larger unit cells than their bulk counterpart.[22,28] An interesting observation is the near-identical relative expansion of the *a*-axis at time points where the phases co-exist. Likewise, the relative expansion of the *c*-axis is similar for goethite and hematite at the phase transition. However, this is not observed at the hematite to strontium hexaferrite phase transition where the relative expansion of the *c*-axis in strontium hexaferrite is approximately twice that of hematite. The resemblances in relative lattice expansion of the phases could be an indication of the structural similarities of the phases further supporting the topotactic phase transition described by Mørch et al. and Cudennec and Lecerf.[20,23] The incorporation of Sr in

the hexaferrite structure could potentially explain the difference in relative lattice expansion of the *c*-axis in hematite and strontium hexaferrite.

The crystallite sizes in Figure 2e) were refined using the "Platelet Vector Size" model with a unique *c*-axis for all iron oxides. It could be argued that it would be more sensible to choose the *b*-axis for goethite, as the unique axis, since goethite often forms laths/needles elongated along this axis.[20] Both models were investigated, and it was concluded that the choice of model did not impact the refinement significantly. Both models gave near-identical agreement factors (see Table S2, Supporting Information), although they initially have different aspect ratios, they follow a similar trend converging to platelet shape over time. The model with a unique *c*-axis for goethite was chosen for simplicity, as the same model was used for hematite and strontium hexaferrite.

The goethite crystallites become increasingly anisotropic with a 30% increase in aspect ratio during the 60 s holding time at 573 K. The *a*/*b*-dimension increases from 20 to 29 nm, while the *c*-axis only increases from 17 to 19 nm. The hematite crystallites are very small during the initial formation at 573 K, less than 10 nm along all dimensions. As the temperature is increased to 873 K and goethite is fully converted, the hematite grows to ≈42 nm along the *a*-axis and ≈25 nm along the *c*-axis. A significant crystallite growth is observed again when the temperature was further increased to 1173 K. The maximum observed crystallite sizes of the hematite crystallites are 98 nm along the *a*-axis and 69 nm along the *c*-axis. The crystallite sizes of hematite start decreasing as strontium hexaferrite becomes the dominant phase. The refined crystallite sizes of strontium hexaferrite are 265 nm along the *a*-axis and 69 nm along the *c*-axis at 160 s. It is important to note that 265 nm is above the resolution limit (≈100 nm) where reliable crystallite sizes can be extracted. The sizes that can be reliably extracted given the experimental conditions are discussed in supporting information. In the given experiment it is similar to what can be reliably extracted from laboratory equipment.[29] The *c*-axis is parallel to the stacking of the close-packed oxygen layers in all three phases. The crystallite growth is hence most significant perpendicular to the stacking of oxygen. The combination of similarities in the crystal structure and the particle morphology enables the synthesis of aligned strontium hexaferrite magnets from anisotropic goethite.

2.3. Texture Investigations

To understand the texture evolution, combined texture, and Rietveld analysis were performed using the software MAUD (Materials Analysis Using Diffraction) ver. 2.992. The 2D diffraction images were directly treated in MAUD with the ImageJ plugin.[30–32] Integration and refinement details are stated in Refinement Details—Texture Investigations in MAUD. The texture was modeled for the iron oxide phases – goethite, hematite, and strontium hexaferrite – using the E-WIMV algorithm with an orientation distribution function (ODF) resolution of 5°.[33] Due to the low reciprocal space coverage, fiber texture was imposed in the model. The reconstructed pole figures from MAUD were loaded into MTEX ver. 5.8.1.[34] where the ODF was recalculated for visualization of pole figures and calculation of texture strength. The results are presented in **Figure 3**.

Figure 3a–c shows the final 2D PXRD pattern integrated azimuthally, the refined model, and the residual, respectively. The variation in azimuthal intensity indicates texture in the sample, for example for the peak at $2\theta = 13.8°$ ($\eta = 60°$ int. = 101, $\eta = 180°$ int. = 57).

Figure 3d–g shows the changes in phase weight percentage, isotropic crystallite size, and texture strength with time and temperature for specific PXRD frames throughout the experiment. Instabilities in the MAUD refinement, when crystallite sizes were refined with anisotropic shape, led to the choice of modeling the crystallite shape isotropically. Figure 3d gives the temperature ramp with dashed lines where the temperature increases. In Figure 3e the weight percentages are given, which correspond qualitatively to those from the sequential refinements.

The isotropic crystallite size, Figure 3f, of goethite is relatively constant at ≈40 nm. For hematite, the crystallite size is ≈13 nm at 573 K, and increases steadily from 51 to 85 nm at 873 K. The crystallite size further increases to 208 nm as the temperature is raised to 1173 K. As strontium hexaferrite becomes the dominant phase the crystallite size of hematite decreases corroborating results from the sequential refinements. The refined strontium hexaferrite crystallite sizes are above the resolution limit of the experiment and absolute reliable sizes cannot be extracted. However, the crystallites appear to grow with increasing sintering time at 1173 K from ≈230 nm (120 s) to ≈730 nm (360 s). A common feature observed in all refined phases is that the isotropic crystallite sizes (from the combined analysis) are greater than the anisotropic crystallite sizes.

The texture strength expresses the sharpness of the ODF and the texture strength varies from one for a completely random-oriented polycrystalline sample to ∞ for a single crystal. Figure 3g shows how the texture strength of the iron oxide phases varies during the experiment. The texture strength of goethite decreases from 1.55 to 1.36 m.r.d. as hematite forms which may be a result of the changes in crystal structure and shape during the de-hydroxylation. The texture strength of hematite initiates at ≈1.19 m.r.d. and increases during the heating to 1.34 m.r.d. This could be explained by Ostwald ripening, dissolution of smaller less well-oriented crystallites, and recrystallization into oriented larger hematite crystals. This corroborates with an increase in hematite crystallite size seen in Figure 3f). The texture strength of strontium hexaferrite likewise increases with time from 1.16 to 1.45 m.r.d. within the ≈180 s of sintering. It should be kept in mind that the analysis was performed on single 2D diffraction images collected with low exposure time (16 ms). Figure 3h) provides the pole figures for goethite, hematite, and strontium hexaferrite. It is observed that all three phases display the same type of texture, with a preferred orientation of the crystallographic *c*-axis parallel to the pressing direction. This is also the ideal texture for producing a well-performing permanent magnet as the *c*-axis aligns with the magnetic easy axis of the hexaferrite phase.[7]

2.4. Electron Backscatter Diffraction Analysis

EBSD was used as a complementary method for studying the texture of the sample, while the method also enabled the

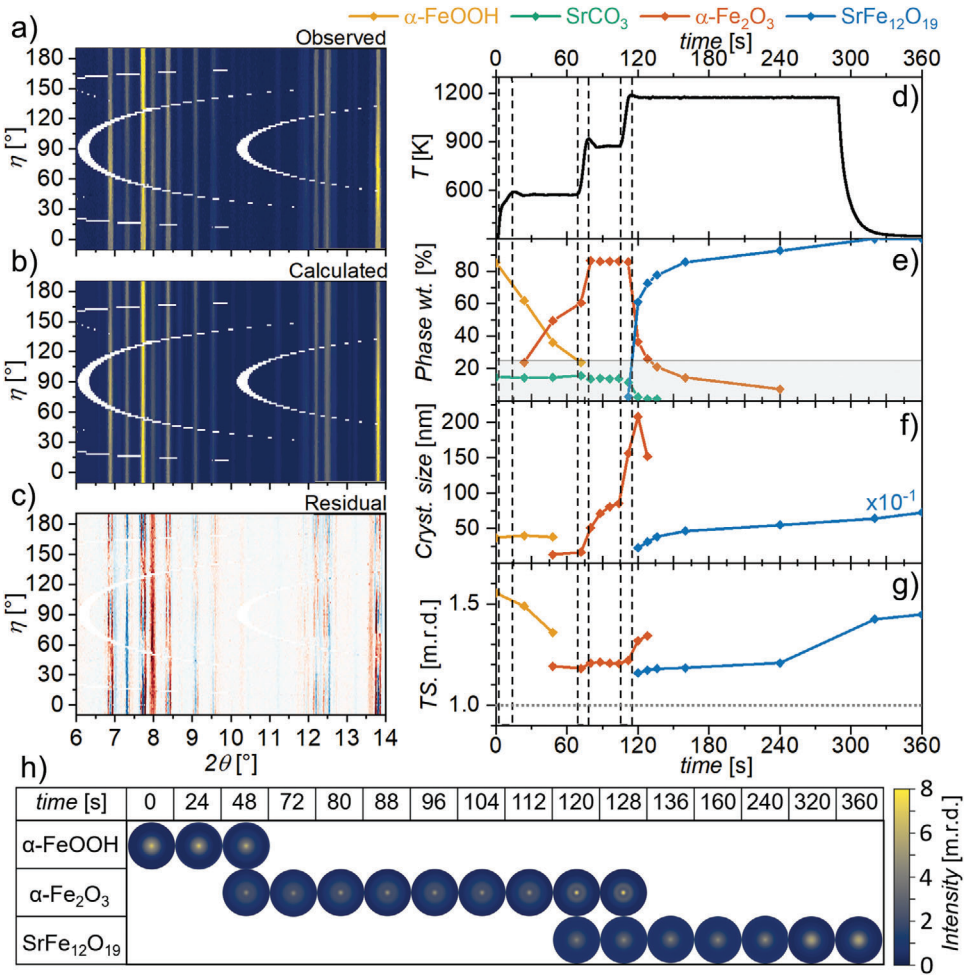

Figure 3. An overview of the results from the combined texture and Rietveld analysis in MAUD. a) azimuthally integrated data of the final PXRD image, and b) the corresponding refined model, both normalized [0,1]. The Cividis colormap has been chosen with dark blue ≤0 and yellow ≥0.8.[35] c) the residual between data and model in percentage going from +15% (red) to −15% (blue). d) the temperature ramp for the duration of the experiment, e) refined phase weight percentages where the color scheme is equivalent to the one used in Figure 2, and f) the isotropic crystallite size, where the $SrFe_{12}O_{19}$ sizes have been multiplied with 10^{-1}. g) texture strength where the dotted gray line indicates random orientation. h) the (00l) pole figures with the pressing direction out of the plane. Only the crystallite size and texture of the major phases (phase percentage >25%) have been included. The refined parameters for the minor phases can be seen in Table S3 (Supporting Information).

estimation of crystallite sizes above 100 nm. In contrast to PXRD where the results represent a global average of a larger sample volume, EBSD probes the sample surface locally allowing for direct visualization of individual grains. The sample preparation and experimental protocol are detailed in Electron Backscatter Diffraction. The micrographs and EBSD maps along with the texture and grain analysis are presented in **Figure 4**. The EBSD map has 76% of the pixels indexed to $SrFe_{12}O_{19}$, while the remaining pixels did not provide solvable electron backscatter patterns. The zero solution pixels mainly lay in grain boundaries and cavities owing to the sample not being 100% dense. The average "mean angular deviation" of the solved pixels is 0.76, which implies a trustworthy indexation.

The stereographic triangle in Figure 4b is the color key to the orientation maps in Figure 4f–h correlating crystal directions to colors. Figure 4a M_s correlates the sample orientation to the coordinate system with the mapped surface (orange) spanned by x and y, with y parallel to the pressing direction. A scanning electron microscopy (SEM) micrograph of the mapped area (red square) is presented in Figure 4c and the band contrast of the EBSD map in Figure 4d provides grain contrast that reveals elongated particles with their long dimension aligned horizontally.

The orientation maps in Figure 4f–h qualitatively show that the [0001] crystallographic direction (red) of the grains, which is parallel to the crystallite c-axis, is predominantly aligned to the pressing direction (y) whereas the $[\bar{1}100]$ (blue) and $[\bar{1}2\bar{1}0]$ (green) directions (which lie in the ab-plane) predominantly are oriented in the xz-plane perpendicular to the pressing direction. Furthermore, the calculated grain boundaries are overlain as black lines. The orientation trend is confirmed by the inverse pole figures in Figure 4i–k calculated from the combined ODF from four maps obtained from different locations on the sample surface (see Figure S9, Supporting Information). They showcase that the crystallographic c-axis is aligned along y while the ab-plane is

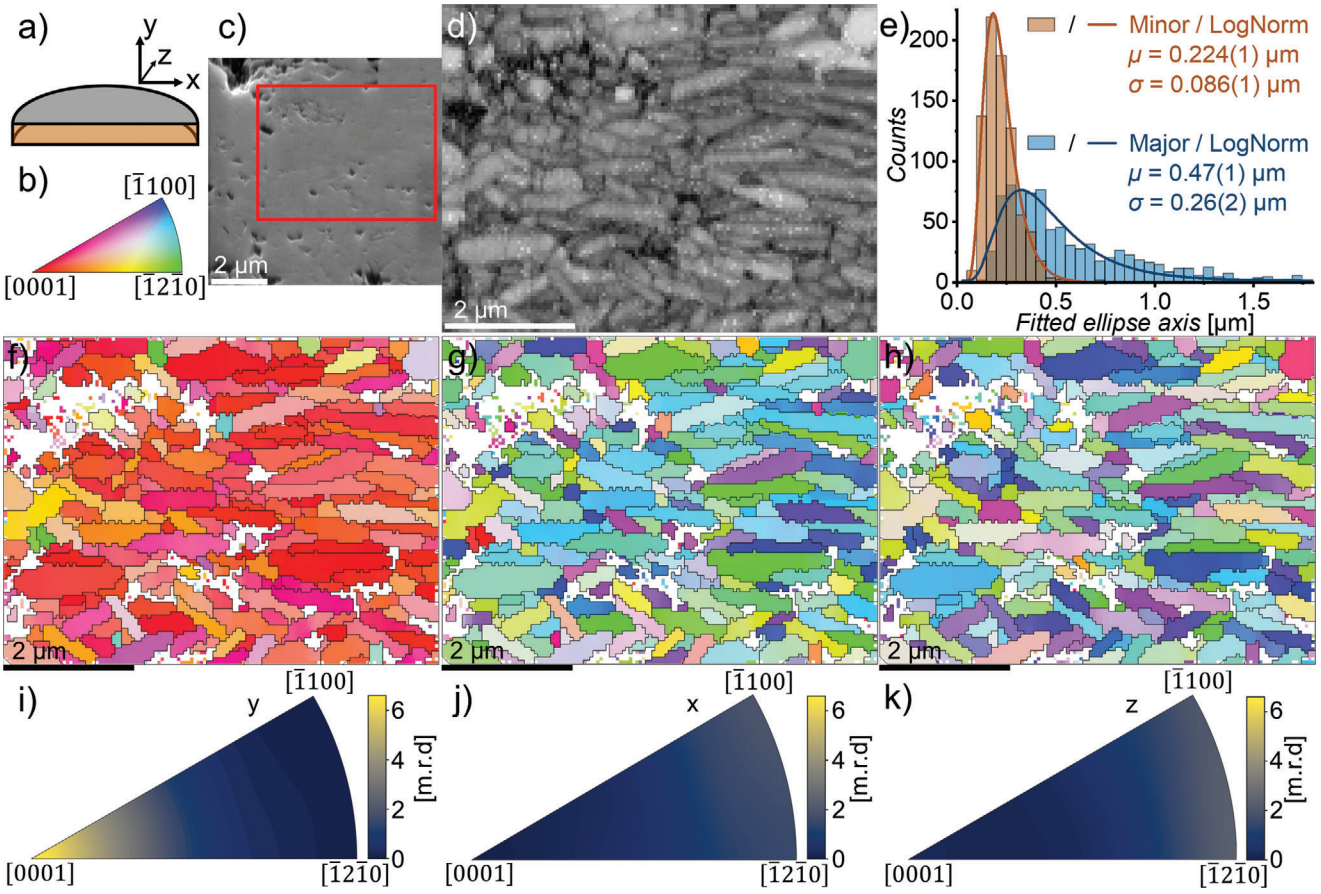

Figure 4. a) Sample sketch correlating the sample dimensions to the coordinate system used in the EBSD maps with mapped cross-section surface marked orange. b) Stereographic color key for orientation maps correlating the colors to the crystallographic directions of $SrFe_{12}O_{19}$. c) SEM image of the surface of the sample, EBSD obtained from the area marked by the red square. d) Band contrast of the EBSD map plotted (greyscale), pixel size 50 × 50 nm. e) Histogram and lognormal distribution of minor and major axis of fitted ellipses of the calculated grains from four EBSD maps. The mean size (μ) and variance (σ) of the fitted distributions are written in the legend. f) Orientation map of $SrFe_{12}O_{19}$ crystal grains with the color key from a) showing the crystallographic direction that points along *y* (parallel to the pressing direction). White areas indicate zero-solution pixels. Calculated grain boundaries are plotted on top as black lines. g) Analog to (f) but showcasing the crystal orientations along *x*. h) Analog to (f) but for the crystal orientations along *z*. i) Inverse pole figure calculated from the total ODF from four EBSD maps, showing the contour of the crystallographic texture along *y* in units of multiples of random distribution [m.r.d]. j) texture along *x*. k) texture along *z*.

predominantly lying in the *xz*-plane. This affirms the decision to choose fiber symmetry in XRD texture analysis. The texture strength calculated from the combined ODF is 1.81 m.r.d., which is comparable to the value from XRD confirming the texture of the sample.

From the EBSD map, it is clear that an elongated morphology is dominating which is consistent with 2D projections of plates aligned along *y*. This is elaborated by fitting ellipses to the calculated grain dimensions from all four maps, excluding grains at the edge of the maps. The angular difference between the orientation of the ellipse major axis and the crystallographic *c*-axis for each grain indicates that the crystallographic texture is correlated with the morphological texture (see supporting information Figure S9, Supporting Information). In Figure 4e the distribution of minor (orange) and major axis (blue) sizes of the fitted ellipses are presented. Most grain sizes are observed to be above the resolution limit of the PXRD peak broadening (>0.1 µm), with a mean size (μ) of 0.47(1) µm and a variance (σ) of 0.26(2) µm of the major axis and μ = 0.224(1) µm and σ = 0.086(1) µm of the minor axis given by the lognormal distributions fitted to the data. The grain dimensions are larger than D_c for $SrFe_{12}O_{19}$ platelets and close to D_c for spherical $SrFe_{12}O_{19}$ (≈0.6 µm), which suggests that the pellet would have a relatively low coercivity.[8,10] The grain analysis is based on the part of the grain that is exposed to the surface. The visible part of a grain may be a fraction of the real grain size.

2.5. Magnetic Hysteresis Curve

The magnetic hysteresis curve for the resulting pellet was measured and the data is shown in **Figure 5**. The insert gives the values of the relevant magnetic properties – M_s (obtained by approach to saturation), M_r, the squareness of the hysteresis curve (M_r/M_s), H_c, and BH_{max}.[36,37]

M_s is intrinsically linked to the atomic structure of the sample and is reduced by impurities. The obtained value 71.01(1) $Am^2\ kg^{-1}$ is reasonably close to the expected M_s of bulk strontium hexaferrite at room temperature, which is

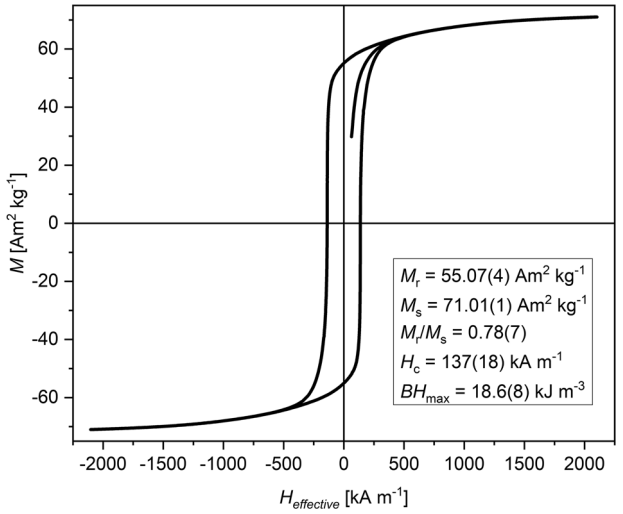

Figure 5. Magnetic hysteresis curve of the resulting magnet. An inset with the magnet properties has been given in the figure.

74.3 $Am^2\ kg^{-1}$.[38] The discrepancy indicates a small impurity, corroborating the weak undescribed peak observed in the PXRD pattern. The squareness of the curve $M_r/M_s = 0.78(7)$ indicates a significant degree of alignment, corroborating the extracted texture strength of 1.45 m.r.d from PXRD. This is comparable with the squareness of other cold compacted magnets, but slightly lower than commercial magnets Y30 and significantly lower than spark plasma sintering (SPS) compacted magnets (see **Table 1**).[10,39] The H_c of 137(18) kA m^{-1} is below the absolute lower limit in H_c for obtaining the theoretical BH_{max}, which is $H_c = ½M_s \approx 180$ kA m^{-1}. The BH_{max} is therefore limited by H_c. The BH_{max} of 18.6(8) kJ m^{-3} is respectable, especially considering the simplicity of the preparation method. The potential BH_{max} can be estimated to $\approx ¼\mu_0 M_r^2 \approx 25$ kJ m^{-3} if H_c could be increased. The BH_{max} is comparable to other hexaferrite magnets made by cold compaction, however, to compete with commercial magnets the BH_{max} must be enhanced (see Table 1). To improve the performance, the crystallite size should be reduced to produce a better H_c and M_r/M_s should be enhanced by improving the texture. Longer annealing time and/or higher temperatures could potentially increase the texture, while adding a grain growth inhibitor, e.g., SiO_2 could limit the crystallite growth to improve H_c. These methods have already been shown to increase the performance of strontium hexaferrite magnets made from cold compacted six-line ferrihydrite.[40]

3. Conclusion

The in situ PXRD experiment has opened the "black box" into sintering of hexaferrite magnets and it was demonstrated that multiple hierarchical length scales with sub-second time resolution can be investigated at elevated temperatures. The study allowed us to investigate length scales that span six orders of magnitude with a 16-ms time resolution. Sequential Rietveld refinements gave insights into the evolution of phases and unit cells, i.e., the atomic structure, and revealed that strontium hexaferrite formed within seconds at ≈1173 K, contrasting the general perception of solid-state reactions being "slow" reactions. Furthermore, following the crystallite sizes on the nanoscale reveals that the anisotropic morphology persisted through the topotactic phase transitions, with the *c*-axis being the shortest crystallographic axis for the iron oxides. Through texture analysis in MAUD, the preferred crystal orientation could be found, revealing the structure on the microscale.

A preferred orientation was observed with the crystallographic *c*-axis parallel to the cold compaction pressing direction, this direction was maintained throughout the phase transitions, from goethite through hematite to strontium hexaferrite. EBSD data supported the preferred orientation observed with PXRD for the hexaferrite phase. Finally, the macroscopic magnetic properties of the sample were determined, revealing that despite the simplicity of the preparation method and the short heating duration, a magnet with good properties was produced.

The presented method can open the "black-box" of calcination and sintering processes and shed light on the chemical processes happening during ultrafast high-temperature sintering. Following rapid calcination can be expanded to other systems and it can significantly speed up the development of advanced functional materials. The technique of using a shaped precursor has potential far beyond magnetic materials and could be significant for other functional materials with directional-dependent properties such as thermoelectric, piezoelectric, and energy storage devices.[41–43]

4. Experimental Section

Precursor Preparation: The goethite (*α*-FeOOH) precursor nanocrystallites were synthesized by employing a hydrothermal synthesis route.[44] A solution of $Fe(NO_3)_3 \cdot 9H_2O$ (1.5 M) was prepared and NaOH (5.0 M) was added dropwise to the nitrate-containing solution under constant magnetic stirring causing the transparent red solution to form a gel-like compound. The $[OH^-]$ to $[NO_3^-]$ ratio was 1:11. The precursor gel was stirred for 15 min. before being transferred to a 1.0 L polypropylene bot-

Table 1. Comparison of the magnetic properties with other strontium hexaferrite magnets from literature and the commercial magnet Y30.

Compaction method	M_s [$Am^2\ kg^{-1}$]	M_r [$Am^2\ kg^{-1}$]	M_r/M_s	H_c [kA m^{-1}]	BH_{max} [kJ m^{-3}]	Refs.
Cold	72.3(1)	59.7(8)	0.83(1)	157(1)	22(5)	[13]
Cold	70.1(2)	-	0.71	297(4)	18(2)	[19]
Cold	69.1(1)	53.9(1)	0.780(1)	195(7)	20.6(4)	[20]
SPS	74.0(10)	67.6(1)	0.93(3)	225	36(4)	[10]
Commercial	74[a)]		0.80–0.89	160–216	26.3–29.5	[39]
Cold	71.01(1)	55.07(4)	0.78(7)	137(18)	18.6(8)	This study

[a)] The saturation magnetization of Y30 is assumed to be 74 $Am^2\ kg^{-1}$.

tle and placed inside an oven for 18 h at 343 K. The resultant product was washed several times until the pH was neutral and was subsequently dried at 343 K for 12 h. The dried α-FeOOH precursor powder was mixed thoroughly with $SrCO_3$ (Strem chemicals, 99.9%) using a mortar and pestle. XRF (X-ray fluorescence Rigaku NEX CG) was used to verify the intended Sr:Fe ratio of 1:10. A hydraulic cold press with a high-carbon steel pressing die and pistons were used to compact the powder (≈50 mg) to a ø≈6 mm pellet using 1.0 GPa for 5 min.

The in Situ Powder Diffraction Experiment: The in situ PXRD experiment was performed at the DanMAX beamline at MAX-IV in Lund, Sweden. The $SrFe_{12}O_{19}$ phase was obtained using the AROS furnace.[2] The cold compacted pellet was placed within a carbon felt strip wherein a small pellet-sized "pocket" had been cut and subsequently sintered rapidly using DC resistive heating. The setup used has been described in detail by Shyam et al.[2] The sample was sintered in an argon atmosphere using the following heating ramp:

$$R.T. \xrightarrow{50\ K\ s^{-1}} 573\ K\ /\ 60\ s \xrightarrow{50\ K\ s^{-1}} 873\ K\ /\ 30\ s \xrightarrow{50\ K\ s^{-1}} 1173\ K\ /\ 180\ s \rightarrow R.T. \quad (1)$$

The pellet surface normal was rotated $\omega = 15°$ with respect to the incident beam to increase the texture information in the data. During heating, 2D diffraction images were continuously collected at 62.5 Hz using a DECTRIS PILATUS X 2M CdTe detector. The X-ray beam energy was 35 keV ($\lambda = 0.354$ Å).

Refinement Details—Sequential Refinements in FullProf Suite: Sequential refinements were performed with the software FullProf Suite.[25] The peak shapes were modeled using the Thompson-Cox-Hastings-Pseudo-Voigt Axial Divergence model, while the background was described by a 6th-degree Chebyshev polynomial. The following parameters were refined: zero displacement, scale factor, unit cell parameters, and overall B-factor. The crystallite sizes were refined using the "Platelet Vector Size" model with the unique axis defined as the *c*-axis. Furthermore, the preferred orientation was also refined using the "Modified March's" function in FullProf Suite. An instrumental resolution file, created by the refinement of a Si 640f NIST standard, was used to model the instrumental contribution to peak broadening.

Refinement Details—Texture Investigations in MAUD: MAUD texture refinements were carried out from 2D diffraction images measured at *time* = 0, 24, 48, 72, 80, 88, 96, 104, 112, 120, 128, 136, 160, 240, 320, and 360 s during the in situ sintering. The 2D diffraction images were integrated into 2° bins with a 2θ step size of 0.02°. The white areas observed in Figure 3a–c are due to the tiling of the detector modules in the PILATUS 2M detector.

An instrumental file, used to estimate sample-to-detector distance and instrumental broadening, was created by first refining a Si 640f NIST standard with a known unit cell to obtain the sample-to-detector distance. Hereafter, a CeO_2 standard with no broadening due to particle size was refined with the sample-to-detector fixed to estimate the instrumental broadening.

A 4th-degree polynomial was used to refine the background. The following parameters were also refined: incident intensity, unit cell parameters, an isotropic thermal vibration factor, and phase fractions of the observed phases. The isotropic crystallite size and microstrain were refined for all phases.

Electron Backscatter diffraction: The sample pellet was demagnetized at 550 °C for 30 min and subsequently cut in half with a diamond wire saw revealing a cross-sectional face parallel to the pressing direction. One fragment was hot-mounted in a conductive resin and carefully ground and polished mechanically by hand with 9, 1, and 0.25 µm diamond paste and 0.04 µm colloidal silica abrasives. The sample was carefully washed with a neutral detergent and wiped multiple times to remove excess abrasive between each polishing step rinsed with ethanol and dried with compressed air.

EBSD mapping was performed on a scanning electron microscope (TESCAN CLARA) with an EBSD system (Oxford Instruments: Symmetry S2 detector and AZtec v6.0 SP2 software). The sample was pre-tilted 70° and measured with 10 kV acceleration voltage and 1 nA current to minimize electron charge drift. Corresponding micrographs were measured with an Everhart-Thornley detector. The EBSD maps were collected with 50 nm pixel size and a frequency between 4 and 20 Hz. The data was exported to MTEX ver 5.10.2.[34] for texture and grain analysis. Four maps from different areas of the sample were collected and combined into a single ODF from which inverse pole figures and the texture strength were calculated. Grain analysis was performed on the same four maps. The threshold for grain boundaries was set to a 5° orientation difference and non-indexed regions were kept with a threshold of the quotient between the number of pixels and the number of boundary segments in a region of 0.65. Grains with less than 6 pixels were discarded. The pixels within the grains were smoothened with a half-quadratic filter. Ellipses were fitted to the grains to estimate the size and orientation of the grains. Grains that border the edge of the maps were excluded from the analysis. The band contrast was retrieved as the intensity in the Kikuchi lines for each electron backscatter pattern.

Magnetic Characterization: Magnetic hysteresis curves were measured using a Physical Property Measurement System with a VSM option from Quantum Design before the sample was cut for EBSD. The sample was placed in a 6 mm brass sample holder and held in place with two quartz rods. The sample was measured in an applied field ranging from ±3 T at 300 K. The measured magnetic hysteresis curve was corrected for (shape) demagnetization by using the infinite slope method.[36,45]

Supporting Information

Supporting Information is available from the Wiley Online Library or from the author.

Acknowledgements

Financial support was obtained from the Independent Research Fund Denmark – Green Transitions COMPASS (1127-00235B). The authors thank the Danish Agency for Science, Technology, and Innovation for funding the instrument center DanScatt (7129-00006B) supporting access to beamtime. The authors acknowledge MAX IV Laboratory for time on Beamline DanMAX. Research conducted at MAX IV is supported by the Swedish Research Council under contract 2018–07152, the Swedish Government Agency for Innovation Systems under contract 2018–04969, and Formas under contract 2019–02496. DanMAX is funded by the NUFI grant no. 4059-00009B. Tommy Ole Kessler and Jeppe Dalgaard Mikkelsen are gratefully acknowledged for the design and engineering of the AROS sample environment. The authors thank Innokenty Kantor for his assistance in using the DanMAX beamline and Jacob L. Valentin, Jesper Simonsen, and Jacob Svane for their participation in the beamtime. Affiliation with the SMART and Q-MAT lighthouse and Centre for Integrated Materials Research (iMAT) at Aarhus University is gratefully acknowledged. The Carlsberg Foundation is acknowledged for funding the TESCAN CLARA SEM and EBSD detector used in this study, CF20-0364 and CF21-0260, while Rebekka Klemmt and Espen Drath Bøjesen are thanked for instrument training.

Conflict of Interest

The authors declare no conflict of interest.

Data Availability Statement

The data that support the findings of this study are available from the corresponding author upon reasonable request.

Keywords

combined texture and Rietveld analysis, electron backscatter diffraction, in situ X-ray diffraction, permanent magnets, strontium hexaferrite, ultrafast sintering

Received: February 5, 2024
Revised: April 5, 2024
Published online:

[1] C. Wang, W. Ping, Q. Bai, H. Cui, R. Hensleigh, R. Wang, A. H. Brozena, Z. Xu, J. Dai, Y. Pei, C. Zheng, C. Pastel, J. Gao, X. Wang, H. Wang, J.-C. Zhao, B. Yang, X. R. Zheng, J. Luo, Y. Mo, B. Dunn, L. Hu, *Science* **2020**, *368*, 521.
[2] P. Shyam, F. H. Gjørup, M. I. Mørch, A. P. Laursen, A. Z. Eikland, I. Kantor, M. R. V. Jørgensen, M. Christensen, *Appl. Mater. Today.* **2023**, *35*, 101960.
[3] J. Ormerod, *Modern Permanent Magnets*, Woodhead Publishing, Sawston, Cambridge **2022**, 403.
[4] H. R. Kirchmayr, *J. Phys. D: Appl. Phys.* **1996**, *29*, 2763.
[5] J. Hölscher, M. Petrecca, M. Albino, P. G. Garbus, M. Saura-Múzquiz, C. Sangregorio, M. Christensen, *Inorg. Chem.* **2020**, *59*, 11184.
[6] A. Xia, C. Zuo, L. Chen, C. jin, Y. Lv, *J. Magn. Magn. Mater.* **2013**, *332*, 186.
[7] R. C. Pullar, *Prog. Mater. Sci.* **2012**, *57*, 1191.
[8] F. H. Gjørup, M. Saura-Múzquiz, J. V. Ahlburg, H. L. Andersen, M. Christensen, *Materialia* **2018**, *4*, 203.
[9] D. L. Leslie-Pelecky, *Chem. Mater.* **1996**, *8*, 1770.
[10] M. Saura-Múzquiz, C. Granados-Miralles, H. L. Andersen, M. Stingaciu, M. Avdeev, M. Christensen, *ACS Appl. Nano. Mater.* **2018**, *1*, 6938.
[11] J. M. D. Coey, *IEEE Trans. Magn.* **2011**, *47*, 4671.
[12] C. J. Fernández, C. Sangregorio, J. Figuera, B. Belec, D. Makovec, A. Quesada, *J. Phys. D: Appl. Phys.* **2021**, *54*, 153001.
[13] J. Thomas-Hunt, A. Povlsen, H. Vijayan, C. G. Knudsen, F. H. Gjørup, M. Christensen, *Dalton Trans.* **2022**, *51*, 3884.
[14] M. Stingaciu, A. Z. Eikeland, F. H. Gjørup, S. Deledda, M. Christensen, *RSC Adv.* **2019**, *9*, 12968.
[15] J. M. D. Coey, *Scr. Mater.* **2012**, *67*, 524.
[16] J. M. D. Coey, *Engineering* **2020**, *6*, 119.
[17] First4Magnets: How are ferrite magnets made?, https://www.first4magnets.com/tech-centre-i61/information-and-articles-i70/ferrite-magnet-information-i83/how-are-ferrite-magnets-made-i104, (accessed: August **2023**).
[18] A. Amato, A. Becci, A. Bollero, M. d. M. Cerrillo-Gonzalez, S. Cuesta-Lopez, S. Ener, I. Dirba, O. Gutfleisch, V. Innocenzi, M. Montes, K. Sakkas, I. Sokolova, F. Veglió, M. Villen-Guzman, E. Vicente-Barragan, I. Yakoumis, F. Beolchini, *ACS Sustainable Chem. Eng.* **2023**, *11*, 13374.
[19] H. Vijayan, A. Povlsen, J. Thomas-Hunt, M. I. Mørch, M. Christensen, *J. Alloys Compd.* **2022**, *915*, 165333.
[20] M. I. Mørch, J. Thomas-Hunt, A. P. Laursen, J. Simonsen, H. Vijayan, M. Christensen, *Chem. Mater.* **2024**, *36*, 1919.
[21] A. B. Jensen, T. E. K. Christensen, C. Weninger, H. Birkedal, *J. Synchrotron Radiat.* **2022**, *29*, 1420.
[22] A. F. Gualtieri, P. Venturelli, *Am. Mineral.* **1999**, *84*, 895.
[23] Y. Cudennec, A. Lecerf, *Solid State Sci.* **2005**, *7*, 520.
[24] S. Nie, Y. Liu, Q. Liu, M. Wang, H. Wang, *Eur. J. Mineral.* **2017**, *29*, 433.
[25] J. Rodríguez-Carvajal, *Phys. B (Amsterdam, Neth.)* **1993**, *192*, 55.
[26] A. R. West, *Solid State Chemistry and its Applications*, Wiley, Chichester, West Sussex **2014**.
[27] U. Schwertmann, R. M. Cornell, *Iron Oxides in the Laboratory – Preparation and Characterization*, Wiley-VCH, Weinheim, Germany, **2000**.
[28] O. M. Lemine, M. Sajieddine, M. Bououdina, R. Msalam, S. Mufti, A. Alyamani, *J. Alloys Compd.* **2010**, *502*, 279.
[29] C. Weidenthaler, *Nanoscale* **2011**, *3*, 792.
[30] C. A. Schneider, W. S. Rasband, K. W. Eliceiri, *Nat. Methods.* **2012**, *9*, 671.
[31] L. Lutterotti, M. Bortolotti, G. Ischia, I. Lonardelli, H.-R. Wenk, Z. Kristallogr, *Suppl.* **2007**, *26*, 125.
[32] L. Lutterotti, MAUD: Materials Analysis Using Diffraction v. 2.992, **2021**.
[33] D. Chateigner, L. Lutterotti, M. Morales, International Tables for Crystallography, **2019**, 555.
[34] F. Bachmann, R. Hielscher, H. Schnaeben, *Solid State Phenom.* **2010**, *160*, 63.
[35] J. R. Nuñez, C. R. Anderton, R. S. Renslow, *PLoS One* **2018**, *13*, e0199239.
[36] F. H. Gjørup, PhD Thesis, Aarhus University, Denmark, **2022**.
[37] J. M. D. Coey, *Magnetism and Magnetic Materials*, Cambridge University Press, Cambridge, England **2009**.
[38] B. T. Shirk, W. R. Buessem, *J. Appl. Phys.* **1969**, *40*, 1294.
[39] Magnetic properties of commercial Y30 ferrite magnet from Magfine, https://www.magfine.it/en/user_data/ferrite_property.php (accessed: September, **2023**).
[40] H. Vijayan, A. Laursen, M. Stingaciu, P. Shyam, F. Gjørup, J. Simonsen, M. Christensen, *ACS Appl. Nano Mater* **2023**, *6*, 8156.
[41] H. Itahara, W.-S. Seo, S. Lee, H. Nozaki, T. Tani, K. Koumoto, *J. Am. Che. Soc.* **2005**, *127*, 6367.
[42] G. L. Messing, S. Trolier-McKinstry, E. M. Sabolsky, C. Duran, S. Kwon, B. Brahmaroutu, P. Park, H. Yilmaz, P. W. Rehrig, K. B. Eitel, E. Suvaci, M. Seabaugh, K. S. Oh, *Crit. Rev. Solid State Mater. Sci.* **2004**, *29*, 45.
[43] J. Zheng, L. A. Archer, *Chem. Rev.* **2022**, *122*, 14440.
[44] A. Malathi, P. Arunachalam, J. Madhavan, A. M. Al-Mayouf, M. A. Ghanem, *Colloids Surf., A* **2018**, *537*, 435.
[45] M. Saura-Múzquiz, C. Granados-Miralles, M. Stingaciu, E. D. Bøjesen, Q. Li, J. Song, M. Dong, E. Eikeland, M. Christensen, *Nanoscale* **2016**, *8*, 2857.